

# Northumbria Research Link

Citation: Agrawal, Prashant, Wells, Gary, Ledesma Aguilar, Rodrigo, McHale, Glen and Sefiane, Khellil (2021) Beyond Leidenfrost levitation: a thin-film boiling engine for controlled power generation. *Applied Energy*, 287. p. 116556. ISSN 0306-2619

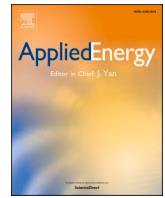
Published by: Elsevier

URL: <https://doi.org/10.1016/j.apenergy.2021.116556>  
<<https://doi.org/10.1016/j.apenergy.2021.116556>>

This version was downloaded from Northumbria Research Link:  
<http://nrl.northumbria.ac.uk/id/eprint/45305/>

Northumbria University has developed Northumbria Research Link (NRL) to enable users to access the University's research output. Copyright © and moral rights for items on NRL are retained by the individual author(s) and/or other copyright owners. Single copies of full items can be reproduced, displayed or performed, and given to third parties in any format or medium for personal research or study, educational, or not-for-profit purposes without prior permission or charge, provided the authors, title and full bibliographic details are given, as well as a hyperlink and/or URL to the original metadata page. The content must not be changed in any way. Full items must not be sold commercially in any format or medium without formal permission of the copyright holder. The full policy is available online: <http://nrl.northumbria.ac.uk/policies.html>

This document may differ from the final, published version of the research and has been made available online in accordance with publisher policies. To read and/or cite from the published version of the research, please visit the publisher's website (a subscription may be required.)



# Beyond Leidenfrost levitation: A thin-film boiling engine for controlled power generation

Prashant Agrawal<sup>a,\*</sup>, Gary G. Wells<sup>a,b</sup>, Rodrigo Ledesma-Aguilar<sup>a,b</sup>, Glen McHale<sup>a,b</sup>, Khellil Sefiane<sup>b</sup>

<sup>a</sup> Smart Materials & Surfaces Laboratory, Faculty of Engineering & Environment, Northumbria University, Newcastle upon Tyne NE1 8ST, UK

<sup>b</sup> School of Engineering, Institute for Multiscale Thermo-fluids, The University of Edinburgh, The King's Buildings, Edinburgh EH9 3LJ, UK

## HIGHLIGHTS

- We present a thin-film boiling engine with a manual control of the power output.
- We support the weight of the rotors and indirectly vary the pressure in the vapor layer.
- We control the power output by changing the gap between the rotor and substrate.
- We achieve about 3.5 times increase in efficiency compared to levitation-based engines.
- An analytical model is used to characterize and explain the rotation.

## ARTICLE INFO

### Keywords:

Thin-film boiling  
Heat engine  
Leidenfrost  
Turbine  
Droplet  
Liquid bridge

## ABSTRACT

Overcoming friction between moving components is important for reducing energy losses and component wear. Hydrodynamic lubrication via thin-film boiling provides an opportunity for reduced friction energy and mass transport. A common example of such lubrication is the Leidenfrost effect, where a liquid droplet levitates on a cushion of its own vapor on a surface heated to temperatures above the liquid's boiling point. An asymmetry in this vapor flow, self-propels the droplet on the surface due to viscous drag, converting thermal energy to mechanical motion, like a heat engine. Although levitation significantly reduces friction, the induced self-propulsion depends on substrate geometry and material properties, which limits dynamic propulsion control. Therefore, the ability to control the power output is a significant challenge in realizing operational mm and sub-mm scale virtually frictionless engines. Here, we present a thin-film boiling engine where we control the power output mechanically. The rotor, which comprises of a working liquid coupled to a non-volatile solid, is manually positioned over a heated turbine-inspired stator in a thin-film boiling state. We show that by controlling the position of the rotor over the substrate the power output from the rotation can be controlled above and below the Leidenfrost temperature (~250 °C). We explain these experimental observations using a hydrodynamic analytical model. Additionally, we achieve propulsion outputs almost 4 times higher than levitation-based propulsion systems. The ability to control the rotation characteristics of such virtually frictionless engines allows potential applications in extreme environments such as at microscales or for space and planetary exploration.

## 1. Introduction

Recent interest and advancements in space exploration has generated a need for technologies that can accomplish in-situ resource utilization on spacecraft and planetary bodies [1]. System scale miniaturization for applications such as, fuel and propellant synthesis

[2,3], planetary terraforming [4,5], regolith processing [6] and, more importantly, energy generation [1,7,8], is also critical to reduce raw and processed material transportation volumes. Energy production in these extreme environments is essential for these applications, wherein, micro- and meso-scale thermomechanical engines [9,10] may provide possible alternatives to traditional photovoltaic, wind and nuclear

\* Corresponding author.

E-mail address: [prashant.agrawal@northumbria.ac.uk](mailto:prashant.agrawal@northumbria.ac.uk) (P. Agrawal).

<https://doi.org/10.1016/j.apenergy.2021.116556>

Received 24 April 2020; Received in revised form 9 January 2021; Accepted 23 January 2021

Available online 13 February 2021

0306-2619/© 2021 The Authors. Published by Elsevier Ltd. This is an open access article under the CC BY license (<http://creativecommons.org/licenses/by/4.0/>).

energy systems.

Micromachining advancements provided breakthrough in miniaturizing established gas and vapor thermodynamic cycles, like Brayton, Otto and Rankine cycles. Development of internal combustion micro engines [11,12], gas turbines [13,14], steam turbines [15] and related micro-components like boilers [16] and micropumps [17,18,19] presented challenges in thermal management [20] and overcoming frictional forces. Due to a high surface area to volume ratio at these small scales, solid friction between moving components introduces significant energy losses and component wear [21,22]. Friction reduction can be achieved by removing contact between a stator and a rotor using levitation via electric [23,24] and magnetic fields [25] or hydrodynamic flows using liquid [26,27] and vapor [28] bearings. Primarily employed for micromotors, such mechanisms generally require multi-component design, small tolerances and complex machining processes, making them unsuitable for thermal energy harvesting.

Another method for providing lubrication with reduced system complexity has been explored via thin-film boiling of a working substance. Most commonly observed as the Leidenfrost effect, where a liquid on contact with a superheated substrate levitates on a cushion of its own vapor [29,30]. The lubrication provided by the vapor layer provides extreme mobility to the levitating liquid droplet (or sublimating solid), which allows propulsion via small forces using externally applied electric [31] and magnetic [32] fields. More significantly, these levitating objects can self-propel by introducing an asymmetry in the vapor flow, either through asymmetrically textured surfaces [33,34,35] or through an asymmetric mass distribution [36,37]. Asymmetric textures like nanorods [38], macro scale ratchets [39,40,41,42,43,44,45,46] and herringbones [34] entrain the vapor asymmetrically that produces a viscous drag on the levitating object, propelling it in a specific direction. In the case of an asymmetric mass distribution, an unbalanced pressure in the vapor layer produces the propulsion force [37]. This simultaneous lubrication and self-propulsion has been used to rotate volatile and non-volatile objects using similar principles through asymmetric mass distributions [37,47,48] and turbine-like textured substrates [49,50]. This thermal energy conversion to mechanical motion illustrates the working of a heat engine, where the thermodynamic cycle is similar to a Rankine cycle, with a key difference that the heat input and work output operations are performed in a single stage, which simplifies system design.

Although thin-film boiling virtually eliminates friction, a significant limitation of these levitation-based engines is the inability to dynamically control their power output. In the thin-film boiling regime, the self-propulsion depends on the thickness of the vapor layer which depends on the operating temperature and, liquid and substrate material properties. The onset of thin-film boiling, i.e. the Leidenfrost temperature, can be controlled by altering the ambient pressure [51,52,53] and the surface wettability [54,55,56]. Additionally, by using superhydrophobic coatings the transition to thin-film boiling can be smoothed [57,58] and liquid propulsion can be observed even below the Leidenfrost temperature [50,59]. However, at the onset of thin-film boiling the rotation outputs become almost temperature invariant [50,59], which inhibits any power control mechanism and also limits the practical efficiency of operation.

In this work, we present a thin-film boiling engine with a manual power output control. We continuously drive a non-volatile solid rotor coupled to a liquid volume held in a thin-film boiling state over a turbine-inspired substrate. We support the weight of the rotor using mechanical bearings, while continuously feeding the evaporating liquid. We show that by adjusting the distance between the rotor and the substrate, we can control the rotation speed over a wide temperature range, above and below the Leidenfrost temperature. In doing so, we identify conditions where we overcome the limits of Leidenfrost propulsion and achieve significantly higher rotation outputs compared to levitation-based engines. Using the analogy of a liquid bearing [27], we employ an analytical model to explain our experimental observations to changes

in the pressure in the vapor layer. The low friction operation of such thin-film boiling engines can be utilized at microscales for thermal energy harvesting, while compatibility with solid and liquid working substances is advantageous for power generation in extreme environments. Such engines are also compatible with different types of liquid and solid working substances which provides opportunities for developing next generation engines for space and planetary exploration.

## 2. Propulsion control concept

Fig. 1 (a) depicts our thin-film boiling engine which comprises of a solid rotor coupled to a liquid, manually positioned in a thin-film boiling state over a turbine-inspired substrate. The thermodynamic cycle of this thin-film boiling engine is similar to a traditional Rankine cycle, where the working substance undergoes phase change in a boiler to produce work output over a turbine. However, a key difference here is that the phase change and work-output operations are performed simultaneously in a single stage (Fig. 1). This in-situ arrangement is favored by the millimetric scale of the device as compared to traditional steam cycles and is beneficial in reducing transportation losses of the working fluid.

In a Rankine cycle the power output depends on the pressure difference between the boiler and the condenser; a higher pressure difference increases the power output. We employ a similar principle here for altering the power output, where the pressure in the liquid working substance is altered by pressing it on the heated substrate, while the condenser is at atmospheric conditions. By moving the rotor mechanically up and down, we alter the available volume of liquid between the rotor and the substrate, to the point where the liquid bulges out of the confined space but does not spill out from the substrate (as depicted in Fig. 1 (a)). The pressure in the liquid will be identified by the dynamics of rotation and the curvature of the deformed liquid-air interface as the liquid bulges out. The theoretical efficiency of this cycle will not exceed the Carnot efficiency ( $\eta_{th} = 1 - T_l/T_h$ ), where  $T_l$  is the temperature of the sink and  $T_h$  is the source temperature. However, the maximum practical efficiency will be determined by the maximum pressure that can be generated by the given device scale at the given operating conditions.

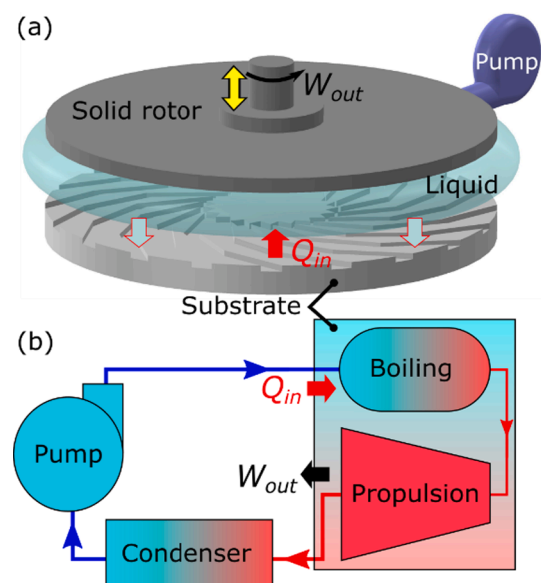


Fig. 1. (a) Depiction of the thin-film boiling engine, comprising of a solid rotor coupled to a liquid working substance by surface tension. The liquid working substance is in a thin-film boiling state over the heated substrate, while the position of the rotor above the substrate can be manually changed. (b) Depiction of the transformation cycle of a working substance in a thin-film boiling engine. The phase-change (boiler) and work output (propulsion/turbine) operations are performed in a single stage on the substrate.

### 3. Experimental method

#### 3.1. Experimental setup

##### 3.1.1. Substrate design

The turbine-inspired substrates are produced by computer numerical control (CNC) machining rectangular grooves in an aluminum substrate, as depicted in Fig. 2 (a). Two different substrates are machined with groove depths ( $D$ ) of 0.1 mm and 0.5 mm and groove width ( $W$ ) of 1 mm. The groove arc is made of 3 straight lines of length 5 mm each oriented at an angle  $\alpha = 45^\circ$  with the center. The radius of the working area of the substrate  $R = 15.05$  mm, the substrate has an additional raised section of width 2 mm and height 1 mm to minimize spillage of the liquid from the working area due to centrifugal forces acting on the liquid volume during rotation. At the operating temperatures above the Leidenfrost temperature the vapor layer between this ring and the liquid removes direct contact [49]. This raised section comprises of grooves, continuing from the substrate geometry, to provide an access to water feed via a needle from a syringe pump (Cole Parmer single-syringe infusion pump). For operation below the Leidenfrost temperature the substrates are made superhydrophobic using a commercial nanoparticle-based spray treatment to reduce friction due to contact line pinning (more details in Supplementary information S3).

##### 3.1.2. Rotor design

The rotor consists of water ( $1\text{--}4\text{ cm}^3$ ) as the liquid working substance, coupled to an aluminum plate ( $R = 15$  mm) through surface tension. The aluminum plate also consists of a shaft (diameter 3 mm and length 10 mm) which is mounted on a z-stage using two ceramic bearings (CCZR-693PK-2PKS, SMB bearings) with outer-diameter 8 mm and inner-diameter 3 mm, as shown in Fig. 2 (b). The z-stage is used to manually alter the gap between the plate and the substrate. Bearing resistance tests are performed before and after each thin-film boiling experiment to assess any significant difference in the bearing performance during the experiment; more details in the Supplementary Information S2. The rotation speed is monitored using a custom-built rotary encoder mounted on the rotor as shown in Fig. 2 (b). The encoder consists of an aluminum foil mounted on the rotor shaft between a photodiode and a LED. The output from the photodiode is recorded on a Raspberry Pi 3 to calculate the time between two instances when the aluminum foil blocks the light from the LED; this time equates to a half rotation. The uncertainty in the measurement from the Raspberry Pi depends on the data acquisition rate and the rotation speed of the rotor. The data acquisition rate of the Raspberry Pi is set at 100 data per second, i.e., a delay of 10-millisecond in the program loop. The corresponding uncertainty in the measured speed at about 30 rad/s is 10.5%. This measurement uncertainty decreases with the rotation speed. For example, the maximum speed recorded in the final rotation experiments is about 18 rad/s, where the measurement uncertainty is 6%. To obtain

the accuracy of the Raspberry Pi measurements, initial experiments were performed where the rotation speed obtained from the microcontroller was compared to speed obtained from side view images of the rotor. A black spot was marked on the side of the rotor, where the number of frames between its occurrence in images, captured using a camera (recording at 100 fps), was used to obtain the rotation speed from the camera images. The maximum difference obtained in the measurements from the microcontroller and the images for over 12 experiments was about 4%.

##### 3.1.3. Bearing resistance estimation

The resistance of the ball bearings is estimated using a spin test. The plate is manually given an initial spin and left to decelerate in ambient conditions (temperature of approximately  $24^\circ\text{C}$ ) to rest. The bearing resistance comprises of a starting torque  $\Gamma_r$  and a dynamic friction term varying with the rotation speed  $\Gamma_\omega$ . The dynamic friction term is proportional to the normal reaction on the balls, which depends on the centrifugal force, therefore,  $\Gamma_\omega = c_\omega \omega^2$ .

The equation of motion of the plate as it decelerates can be written as:

$$I_p \dot{\omega} = -\Gamma_r - c_\omega \omega^2, \quad (1)$$

where,  $I_p$  is the moment of inertia of the aluminum rotor,  $\omega$  is the angular speed of rotation and  $c_\omega$  is the coefficient of the dynamic friction. With an initial condition of  $\omega = \omega_{max}$  at  $t = 0$ , the solution to Eq. (1) is:

$$\text{atan}\left(\frac{\omega}{\omega_r}\right) = \text{atan}\left(\frac{\omega_{max}}{\omega_r}\right) - \frac{\omega_r c_\omega t}{I_p}, \quad (2)$$

where  $\omega_r = \sqrt{\Gamma_r/c_\omega}$ . The experimental data of the speed against time is fitted with Eq. (2) to obtain the fitting parameters  $\omega_r$  and  $c_\omega$  (Fig. 2 (c)). The starting torque is then obtained as:  $\Gamma_r = c_\omega \omega_r^2$ .

#### 3.2. Experimental procedure

The substrate is heated over a hot plate (Stuart UC 150) at the desired temperature and the temperature of the substrate is monitored using a K-type thermocouple in contact with the substrate at the side. Before starting the thin-film boiling experiments, the rotor is given an initial spin to estimate its frictional torque in ambient conditions at the start of the experiment. A fixed volume of water is deposited on the substrate, which reduces the monitored temperature by about  $10\text{--}20^\circ\text{C}$ . A continuous flow of water from the syringe pump is initiated at a flow rate that is pre-calibrated for each temperature. The aluminum rotor is then lowered using the z-stage to contact the liquid until it starts rotating. During this process there might be ejection of droplets from the gap between the plate and the substrate, which changes the volume of the liquid over the substrate from the initially deposited volume. A side

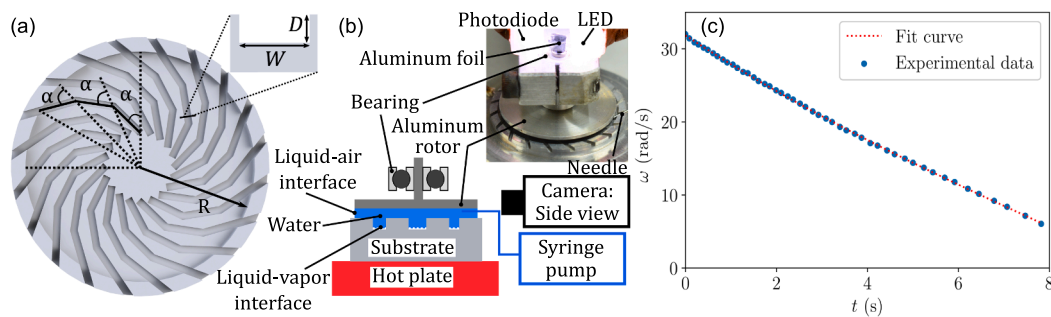


**Fig. 2.** (a) Depiction of the substrate geometry used in the experiments with rectangular cross-section grooves of width  $W$  and depth  $D$  arranged in a turbine-inspired spiral geometry composed of 3 straight sections. (b) Depiction of the experimental setup with the aluminum rotors supported by a bearing assembly. The rotation is measured using a custom-built encoder. (c) Variation of speed with time of the rotor as it decelerates to rest during the spin experiment. Eq. (2) is fitted to the data to measure the resistive torque from the bearings.

view of the rotors is monitored using a camera (UI-3130LE, IDS imaging systems) to measure the gap between the plate and the substrate, and the liquid rotor configuration over time. The temperature of the substrate is monitored throughout the experiment and is observed to vary within  $\pm 5$  °C. At the end of the experiment, the rotor is lifted from the substrate and the bearing resistance measurement procedure is repeated to measure its resisting torque at the end of the experiment. The rotor is then left over the hot plate for about 900–1200 s to vaporize the condensate in the bearings. In this unsealed experimental setup, the condensate is observed to increase the bearing resistance over the duration of the experiment; more details in the Supplementary Information S2. The rotor assembly is then removed from the hot plate and left to cool down for about 1200–1800 s in ambient conditions before starting the next experiment. The frictional torque from the bearings, for one experiment, is taken as an average of the values obtained from the spin tests before and after the respective experiment. This experimental protocol is developed after conducting several tests on the bearing performance under different conditions, as described in Supplementary Information S1.

#### 4. Experimental results

A typical rotation sequence of the rotor, starting from rest is shown in Fig. 3 (a). As mentioned in Section 3.2, once the aluminum rotor is coupled to the water over the substrate (Fig. 3 (a) (i)), the rotor is lowered even further till rotation is initiated (Fig. 3 (a) (ii)). The rotor accelerates from rest due to the driving torque from the vapor and is

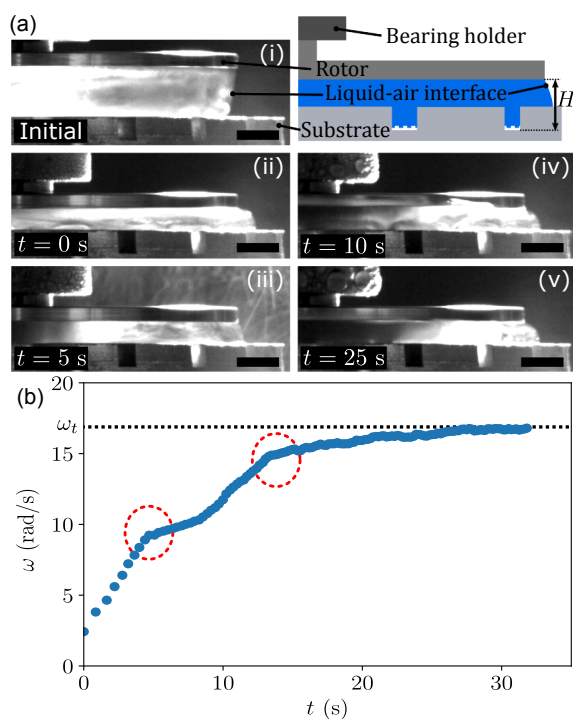


**Fig. 3.** (a) Image sequence of rotation of the couple aluminum rotor and water over the substrate, with a depiction of the liquid and solid rotor configuration over the substrate. The rotation starts after the liquid is pressed against the heated substrate heated at  $T = 325$  °C. The groove depth  $D = 500\mu$  m and the flow rate for stable rotation is  $19 \text{ mm}^3/\text{s}$ . The black line on the bottom right represents the scale bar (3 mm). Droplets ejected from the gap between the rotor and substrate vaporize after falling on the hot plate and are seen as mist and small droplets in (iii). (b) Variation of angular speed of the rotor with time. The droplet ejection events are indicated by dashed red lines and are accompanied by sudden variations in the angular acceleration of the rotors (experimentally observed in (a) (iii) at  $t = 5$  s). Videos of rotation are provided in supplementary videos ‘SV1.avi’ and ‘SV2.avi’.

resisted by the inertial resistance due to the liquid deformation in the grooves [34] and the friction in the bearing. The rotor eventually attains a terminal (constant) angular speed ( $\omega_t$ ) when the resistance to rotation balances the driving torque (Fig. 3 (b)). The rotor undergoes abrupt changes in its acceleration to a terminal speed, as seen in the data in Fig. 3 (b) at around  $t = 5$  and  $t = 13$  s. These abrupt changes in the rotation speed coincide with droplet ejection events from the gap between the substrate and the rotor as observed around the time  $t = 5$  s in Fig. 3 (a) (iii).

As the rotor accelerates, centrifugal force on the liquid increases, pushing the liquid towards the circumference, where spillage is minimized due to the designed 1 mm raised section in the substrate. A vapor bubble also forms at the center due to a high pressure in the vapor layer [60,61]. This bubble size depends on the scale of the substrate, substrate design and the centrifugal force due to rotation [50]. The bubble de-wets the liquid from the rotor and redistributes it towards the circumference in the shape of a ring, aiding the droplet ejection process. For a specific volume of liquid between the gap, at a critical speed the liquid overcomes the surface tension at the liquid–air interface (on the side) and breaks out of the liquid volume as a droplet. In the Fig. 3 (a) (iii) this droplet ejection event is seen as a mist and small droplets due to the spontaneous explosive boiling of the ejected droplet when it contacts the surrounding area on the hot plate.

Due to this droplet ejection event the liquid volume over the substrate at terminal speed is different from the initial conditions at which the rotation starts. This is qualitatively observed in Fig. 3, where at  $t = 5$  s, i.e. just after the droplet ejection, the radius of curvature at the liquid–air interface is larger than at  $t = 0$  s. The radius of curvature then decreases as the plate further accelerates and centrifugal forces push the liquid out. It is observed that the terminal speed of rotation depends on the radius of the curvature across all the gaps between the rotor and substrate (Fig. 4). For a given gap  $H$ , a configuration with a smaller radius of curvature ( $R_1 < R_2$ ) shows a higher terminal speed compared to the case with a higher radius of curvature (Fig. 4 (b)).

As the timing and the volume of the ejected droplet is variable, the radius of curvature at the terminal speed of rotation is not controlled. To maintain consistency in the analysis across different gaps and temperatures we consider only the experiments where the radius of curvature is between  $0.5H$  and  $0.7H$ . For these experiments Fig. 5 shows the variation of terminal angular speed with different gap  $H$  for different operating temperatures  $T$ . As the gap between the rotor and the substrate decreases, the terminal speed of rotation is observed to increase. The variation with temperature at a given gap does not follow any specific trend, and is mostly invariant, which agrees with previous observations in a freely levitating rotor [50,59]. For smaller gaps the maximum terminal speed saturates, which may be due to the large size of the vapor bubble in these small liquid volumes that leads to a significant torque loss, due to reduced liquid coverage over the substrate. The droplet ejection event is observed at all gaps as at large gaps the Laplace pressure is insufficient to hold the liquid, while at smaller gaps the increased centrifugal forces (due to higher speeds) aid droplet break-up.

The increase in terminal speed of rotation with decrease in  $H$  can be attributed to the reduction in liquid viscous dissipation due to a lower volume of available liquid for torque transfer from the vapor layer to the solid rotor. However, experiments with a freely levitating rotor on the same substrate design do not show any significant differences in the terminal speed or torque for similar values of gap between the solid plate and the substrate (indicated by the band thickness) [50]. Therefore, the mechanical control of  $H$  is altering the torque generated from the vapor layer, which will be discussed in the following Section 5. We also observe a significant enhancement in the terminal speed of rotation compared to freely levitating rotors, despite the added solid friction from the bearing (Fig. 5).

Fig. 6 shows an example of dynamic control of the rotation speed with changing gap between the rotor and the substrate. After every change in the gap between the rotor and the substrate, the total volume

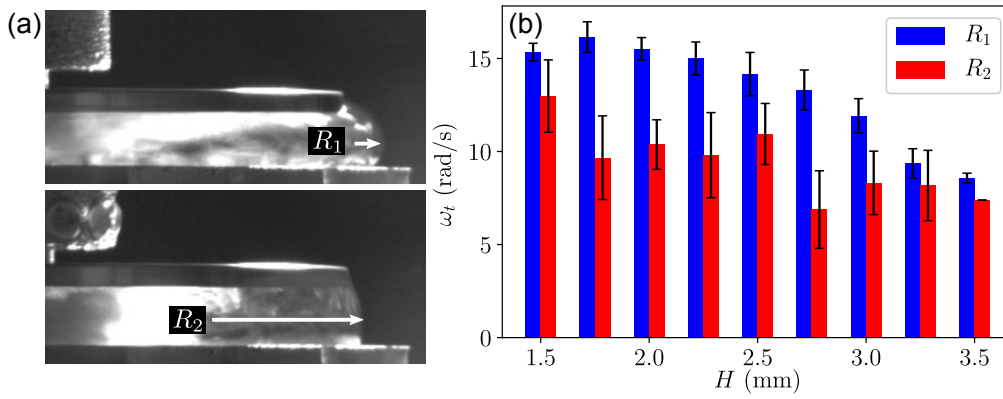


**Fig. 4.** The effect of liquid curvature on the terminal angular speed. (a) Images of two rotor configurations for the same gap between the plate and the substrate with  $R_1 < R_2$ . (b) Variation of terminal angular speed with different gap between the plate and the substrate  $H$  for the two rotor configurations. At the same gap between the substrate and the rotor, a higher radius of curvature of the liquid-air interface ( $R_2$ ) results in a lower terminal angular speed compared to a smaller radius of curvature ( $R_1$ ).

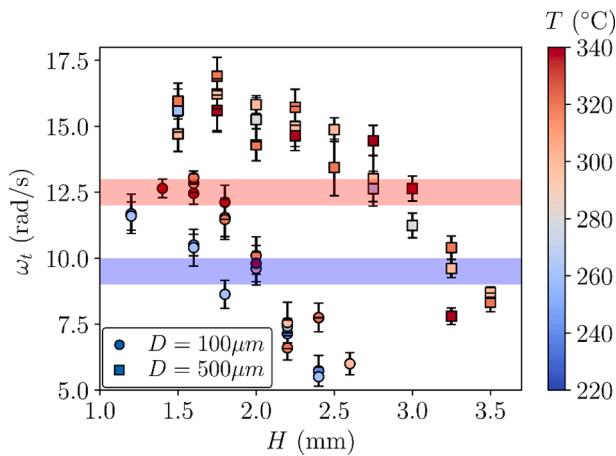


**Fig. 5.** Variation of terminal angular speed with gap for different temperatures for the substrates with  $D = 100 \mu\text{m}$  and  $D = 500 \mu\text{m}$ . The shaded red and blue regions represent the terminal angular speed obtained with a freely levitating rotor for  $D = 500 \mu\text{m}$  and  $D = 100 \mu\text{m}$ , respectively [50]. The color bar on the right indicates the substrate temperature ( $T$ ).

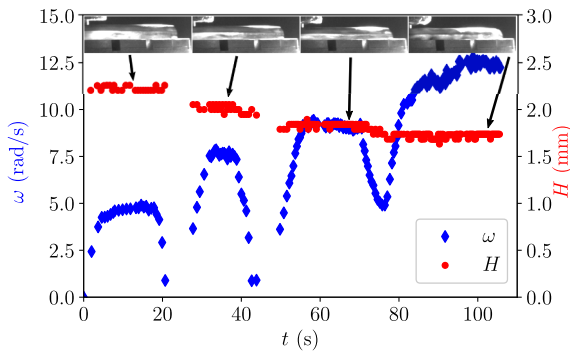


**Fig. 6.** Variation of the rotation speed with changing gap between the rotor and the substrate for a substrate with  $D = 100 \mu\text{m}$ . The temperature of the substrate is  $320^\circ\text{C}$ .

available between the rotor and the stator changes, which leads to the ejection of water droplets from the side. As a result of this change in water volume, the rotation speed decreases momentarily before accelerating to the terminal speed for the new rotor-stator configuration.

It is important to note that the rotation characteristics of this system can be fully characterized by two parameters: starting torque ( $\Gamma_v$ ) and terminal angular speed ( $\omega_t$ ). The terminal angular speed is directly measured from the experiments, while the torque can be obtained from

the angular speed vs time curve by a linear fit at time  $t = 0$ . However, as the droplet ejection timing and volume is random, in most cases there is not enough data resolution near  $t = 0$  to provide an accurate comparative value for torque. Therefore, we rely on the terminal angular speed as an indirect measure of the torque as will be discussed and derived in Section 5.

## 5. Analytical model and discussion

### 5.1. Analytical model

As mentioned in the experimental results in Section 4, the rotation of the liquid and solid is driven by a torque from the vapor layer and resisted by inertia of the liquid deforming over the substrate grooves (Fig. 7). The rotor motion is also resisted by the friction in the bearings that connect the rotors with the z-stage. Considering these torques, the equation of motion of the rotation can be written as:

$$I\dot{\omega} + c_i\omega^2 = \Gamma_v - (\Gamma_r + c_\omega\omega^2) \quad (3)$$

where,  $I$  is the moment of inertia of the combined liquid and solid rotor,  $c_i$  is the coefficient of inertial resistance due to the liquid deformation over the grooves and  $\omega$  is the angular velocity of the rotor assembly. The solution to Eq. (3) can be written as:

$$\omega = \omega_t \tanh(t/\tau), \quad (4)$$

where  $\omega_t$  is the terminal speed of rotation given by:

$$\omega_t = \sqrt{\frac{\Gamma_v - \Gamma_r}{c_i + c_\omega}}, \quad (5)$$

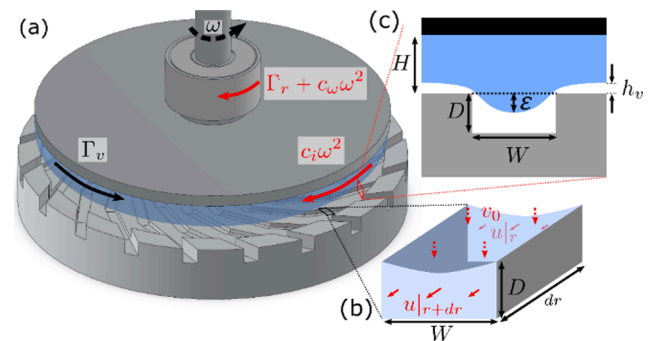


**Fig. 7.** (a) Depiction of the different torques acting on the rotor: (b) driving torque  $\Gamma_v$  from the vapor flow rectification, (c) inertial resistance  $c_i\omega^2$  due to liquid deformation and static and dynamic friction,  $\Gamma_r$  and  $c_\omega\omega^2$ , respectively, from the bearing.  $\epsilon$  is the deformation of the liquid volume into the rectangular grooves.

and  $\tau$  is the relaxation time, which is indicative of the rotor acceleration, given by:

$$\tau = \frac{I}{\sqrt{(\Gamma_v - \Gamma_r)(c_i + c_\omega)}} \quad (6)$$

For the turbine geometry used in the experiments the flow in the grooves is driven by the evaporative flux  $v_0$  (Fig. 7 (b)). Assuming thermal conduction as the dominant mode of heat transfer through the vapor layer and that the heat goes into phase change of the liquid, the evaporative flux can be written as  $v_0 = k\Delta T/(h_v\rho_v L)$ , where  $k$  is the thermal conductivity of the vapor layer,  $\Delta T$  is the temperature difference between the substrate and the boiling point of the liquid,  $\rho_v$  is the density of the vapor,  $L$  is the latent heat of vaporization of the liquid and  $h_v$  is the vapor layer thickness. Assuming a Poiseuille-Couette flow in the rectangular cross-section grooves, the torque due to the viscous stresses from the vapor entrainment (indicated by the vapor flow velocity  $u$  in Fig. 7 (b)) can be written as [50]:

$$\Gamma_v = \frac{2c_i\mu_v N W k \Delta T R^3}{\rho_v L h_v^3} \quad (7)$$

where  $c_t$  is a geometric parameter of the turbine,  $\mu_v$  is the dynamic viscosity of the vapor layer and  $N$  is the number of grooves. The terminal angular speed of rotation can be written as:

$$\omega_t = \sqrt{\frac{\frac{2c_i\mu_v N W k \Delta T R^3}{\rho_v L h_v^3} - \Gamma_r}{c_i + c_\omega}} \quad (8)$$

Apart from  $h_v$  and  $c_i$  all other parameters in Eq. (8) are either material properties or design parameters that are held constant while changing the gap between the rotor and the substrate in the experiments. Here  $c_i = \rho_l \varepsilon R^4 N \sin(\alpha)$ , where  $\varepsilon$  is the liquid deformation in the groove (Fig. 7 (c)),  $\rho_l$  is the liquid density and  $\alpha$  is depicted in Fig. 2. As the liquid is always in a thin-film boiling state, we assume  $\varepsilon$  to be constant and, therefore, the coefficient of inertial resistance  $c_i$  to be independent of  $H$ . Therefore, we look at the factors on which the vapor layer thickness  $h_v$  depends.

For a drop levitating on a substrate, the weight of the droplet balances the average pressure in the vapor layer ( $P_v$ ). The vapor layer thickness is obtained from this pressure balance using the lubrication approximation as [49]:

$$h_v = \left[ \frac{3\mu_v k \Delta T R^2}{2P_v L \rho_v} \right]^{1/4} \quad (9)$$

For a droplet with radius greater than the capillary length ( $l_c$ ),  $P_v = 2\rho_v g l_c$ . In this case the only controllable parameter in Eq. (9) is temperature. In our present system, we remove this weight dependency of the pressure in the vapor layer by supporting the weight of the rotors

using bearings. In this configuration, the coupled liquid–solid rotor configuration resembles a liquid bridge between parallel plates with a pinned contact line as shown in Fig. 8 (a). In this liquid bridge the average normal pressure on the plates comprises of the Laplace pressure, dependent on the radius of curvature of the liquid air interface ( $R_c$ ), and the contact line tension dependent on the contact angle  $\theta_l$  [62]:

$$F_n = -\pi R^2 \frac{\gamma_{la}}{R_c} + 2\pi R \gamma_{la} \sin\theta_l \quad (10)$$

The negative sign in Eq. (10) implies a repulsive force on the plates. In a thin-film boiling configuration the bottom plate is replaced by the vapor layer, as depicted in Fig. 8 (b). At this liquid–vapor interface, the contact angle  $\theta_l = 180^\circ$ . Therefore, from Eq. (10), the average pressure at the liquid–vapor interface can be written as  $F_n/\pi R^2$ , i.e.,  $P_v = \gamma_{la}/R_c$ . Accordingly, using Eq. (9) in Eq. (7), the torque from the vapor rectification depends on the radius of curvature as  $\Gamma_v \propto 1/R_c^{3/4}$  and  $\omega_t \propto 1/R_c^{3/8}$ , assuming a constant  $c_i$ . This correlation qualitatively agrees with the experimental observations in Fig. 4. For the same gap  $H$ , a smaller radius of curvature results in a larger terminal speed of rotation. Similarly, in Fig. 5, a smaller gap for  $\theta_u \approx 180^\circ$  results in a small  $R_c$  and, therefore, a higher terminal speed of rotation.

For a quantitative comparison with the experimental data in Fig. 5, we consider the case of  $\theta_u \approx 180^\circ$ , i.e. where  $R_c \approx H/2$ . Considering that the rotation of the liquid volume adds a pressure due to the centrifugal forces, the pressure at any radial distance  $r$  from the rotation axis can be written as:

$$p = \frac{2\gamma_{la}}{H} - \frac{1}{2}\rho_w(R^2 - r^2)\omega_t^2, \quad (11)$$

where  $\rho_w$  is the density of water. The average pressure in the liquid can be estimated by  $P_v = \int_0^R p 2\pi r dr$ . The vapor layer thickness from Eq. (9) is obtained as:

$$h_v = \left[ \frac{3\mu_v k \Delta T R^2}{2(2\gamma_{la}/H - \rho_w \omega_t^2 R^2/4)L\rho_v} \right]^{1/4} \quad (12)$$

Using Eq. (12) in Eq. (7), the torque from the vapor layer is obtained as:

$$\Gamma_v = c_\Gamma \Delta T^{1/4} \left( \frac{2\gamma_{la}}{H} - \frac{\rho_w \omega_t^2 R^2}{4} \right)^{3/4}, \quad (13)$$

where  $c_\Gamma$  is the coefficient containing all other constant parameters. Using Eq. (13), Eq. (5) can be rewritten as

$$\omega_t^2 = \frac{c_\Gamma}{c_i} \Delta T^{1/4} \left( \frac{2\gamma_{la}}{H} - \frac{\rho_w \omega_t^2 R^2}{4} \right)^{3/4} - \frac{\Gamma_r}{c_i} \quad (14)$$

Considering a first order approximation, Eq. (14) is written as:

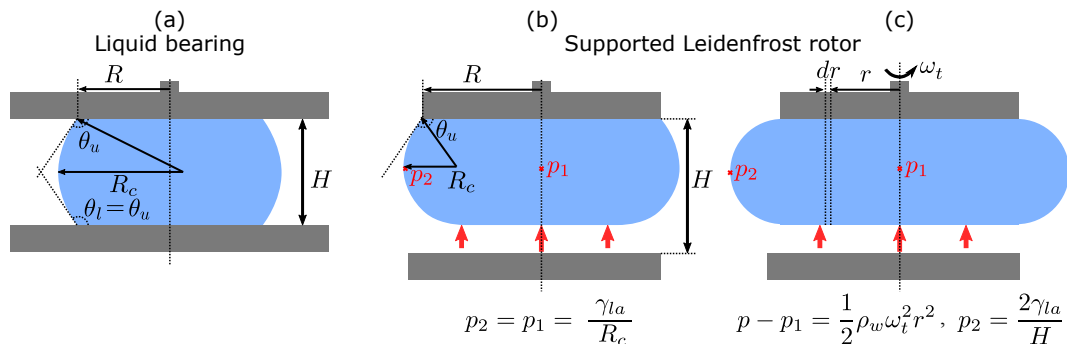


**Fig. 8.** (a) Depiction of an axisymmetrically pinned liquid volume between two parallel plates. The liquid volume adopts a dynamic contact angle  $\theta_u = \theta_l$  and a radius of curvature  $R_c$  for a given separation  $H$ .  $\theta_u$  denotes the dynamic contact angle at the top plate and  $\theta_l$  denotes the dynamic contact angle at the bottom plate. (b) Equivalent configuration of a Leidenfrost drop coupled to a solid plate, where the bottom plate is replaced by the vapor layer. (c) Altered pressure distribution in a Leidenfrost rotor due to centrifugal forces.

$$\omega_t^2 = (2\gamma_{la})^{3/4} \frac{c_r}{c_i} \frac{\Delta T^{1/4}}{H^{3/4}} \left( 1 - \frac{3\rho_w R^2 H \omega_t^2}{32\gamma_{la}} \right) - \frac{\Gamma_r}{c_i} \quad (15)$$

Rearranging Eq. (15),  $\omega_t^2$  is obtained as:

$$\omega_t^2 = \frac{(2\gamma_{la})^{3/4} c_i \frac{\Delta T^{1/4}}{H^{3/4}} - \Gamma_r}{\left[ c_i + \frac{3c_r \rho_w R^2 \Delta T^{1/4} H^{1/4}}{16(2\gamma_{la})^{1/4}} \right]} \quad (16)$$

Eq. (16) is fitted to the experimental data to obtain the coefficients  $c_r$  and  $c_i$  considering an average bearing resistance of  $\Gamma_r = 0.5 \mu\text{Nm}$  (Supplementary information S2) as shown in Fig. 9 (a). The equation is not fitted on the data points for the smallest  $H$  in Fig. 5 as the terminal speed decreases considerably because of the formation of the vapor bubble, which has not been considered in the model. Also, cases where  $H > l_c$  have also been excluded considering the exclusion of gravity in the analytical model. After obtaining  $c_r$  Eq. (13) is used to estimate the torque from the vapor layer.

As observed in Fig. 9 (a), the experimental data for the two substrate geometries agrees well with the trend of Eq. (16) for the considered temperature and gap ranges. To validate the values of the fitting parameters, we first compare the values of the torque obtained analytically with the experimental observations (Fig. 9 (b)). As was mentioned in Section 4, the experimental values are obtained by a linear fit on the

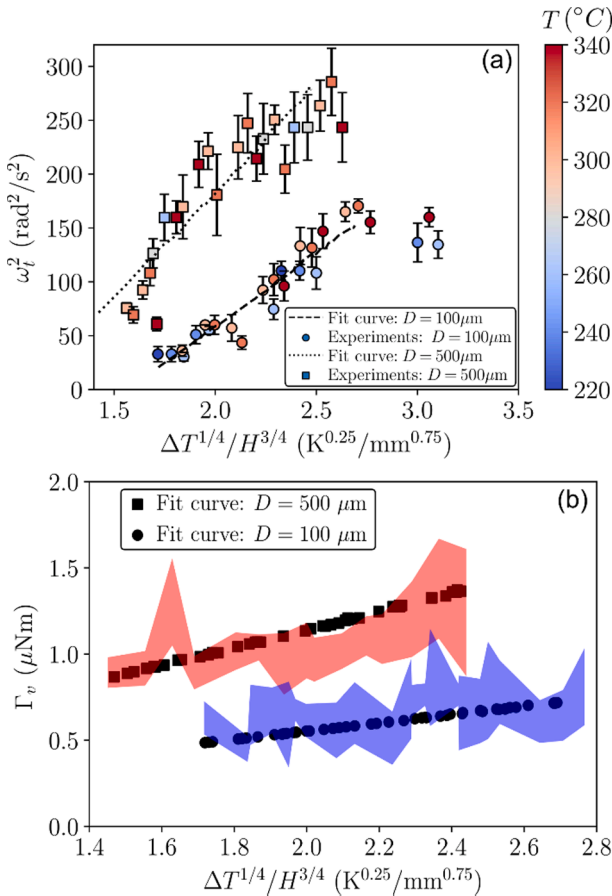


Fig. 9. (a) Eq. (16) fitted to the experimental data for different substrate temperatures  $T$  (color bar on the right) and gap between the rotor and the substrate  $H$  for the two substrate geometries:  $D = 100 \mu\text{m}$  and  $D = 500 \mu\text{m}$ . (b) Comparison of the torque obtained from Eq. (13) with the experimentally observed torque from the linear fit on the speed vs time data (Fig. 3). The shaded regions indicate the experimental data within one standard deviation of the respective mean values for the substrates with  $D = 100 \mu\text{m}$  (blue) and the  $D = 500 \mu\text{m}$  (red). The bearing resistance torque  $\Gamma_r$  is added to the experimentally obtained values to obtain the torque from the vapor layer.

speed vs time data at  $t = 0$ , which, due to droplet ejection, varies significantly and is inappropriate for assessing scaling laws (as is evident by the large error in the data in Fig. 9 (b)). Nevertheless, the values of the torque from the vapor layer from the model agree with the scale of torque observed experimentally. As an additional validation the value of the coefficient of inertial resistance  $c_i$  obtained from the analytical model ( $c_i = 1.8 \times 10^{-9} \text{ kgm}^2$  for  $D = 100 \mu\text{m}$  and  $c_i = 2.8 \times 10^{-9} \text{ kgm}^2$  for  $D = 500 \mu\text{m}$ ) agrees with the scale of  $c_i$  obtained in the case of a freely self-levitating rotor [50] ( $c_i = 1.7 \pm 0.4 \times 10^{-9} \text{ kgm}^2$  for  $D = 100 \mu\text{m}$  and  $c_i = 3.2 \pm 0.6 \times 10^{-9} \text{ kgm}^2$  for  $D = 500 \mu\text{m}$ ). The value of  $c_i$  is smaller for  $D = 100 \mu\text{m}$  as the liquid–vapor deformation in the grooves is smaller than in the case of  $D = 500 \mu\text{m}$  substrate geometry.

## 5.2. Propulsion in the ‘cold’ Leidenfrost regime

Above the Leidenfrost temperature there is a distinct vapor layer between the substrate and the liquid–vapor interface (as depicted in Fig. 10). As seen in the previous sections, by indirectly changing the pressure in the vapor layer, by changing the gap  $H$ , the terminal speed increases with a decrease in  $H$ . However, the opposite trend is observed for propulsion below the Leidenfrost temperature (Fig. 10), i.e., the terminal rotation speed decreases with  $H$  (Fig. 10). In this ‘cold’ Leidenfrost regime [63] the liquid interface minimally contacts the superhydrophobic surface to support the applied pressure (including the gravitational head and capillary pressure). In this configuration, as the pressure is increased (by decreasing  $H$ ), two effects might occur: (1) the increased pressure increases the contact area of the liquid with the substrate, which increases the contact line friction, and (2) the increased pressure pushes and increases the deformation of the liquid–vapor interface in the substrate grooves, increasing the inertial resistance. Both these effects will act to decrease the speed of rotation, as is observed experimentally in Fig. 10. As mentioned in Section 4, due to the dynamic redistribution of the liquid, the starting torque cannot be measured directly. Therefore, we can only qualitatively estimate the power output scale and variation in this low temperature regime from these terminal angular speed plots.

## 5.3. Power output and efficiency

By controlling the power output, we can identify optimum operating conditions across a wide temperature range, spanning two different vapor film regimes. It is also useful here to compare the power outputs of these bearing supported thin-film boiling engines with levitation based (or self-supported) thin-film boiling engines [50]. In these experiments,

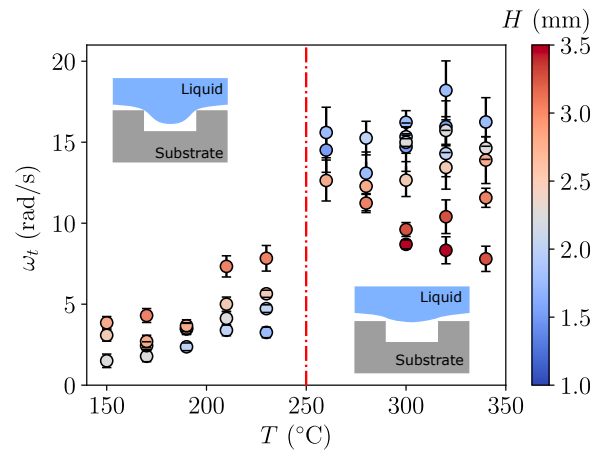


Fig. 10. Variation of terminal speed of rotation with substrate temperature above and below the Leidenfrost temperature (dashed red line) for substrate with  $D = 500 \mu\text{m}$ . The colorbar on the right indicates the gap between the rotor and the substrate  $H$  in millimeters.

levitation-based engines represent the lower limit of the applied pressure as they involve the gravitational pressure head only.

Below the Leidenfrost temperature, as the pressure in the vapor layer is insufficient to support the applied pressure, the vapor layer thickness remains almost invariant with temperature and thus the average pressure in the vapor layer increases linearly with  $\Delta T$  (Eq. (9)) until the Leidenfrost point. In the case of levitation, as the vapor layer thickness remains constant in this regime, from Eq. (7),  $\Gamma_v \propto \Delta T$ ,  $\omega_t \propto \Delta T^{1/2}$  and the average power output  $P_o = \Gamma_v \omega_t / \sqrt{3}$  is proportional to  $\Delta T^{3/2}$  (Fig. 11). As adding more pressure in the bearing supported thin-film boiling engine decreases the rotation speed, the rotation speed (and hence, the power output) obtained is lower than that in the levitation-based engine (Fig. 11 (a)). Therefore, below the Leidenfrost point, levitation-based propulsion provides the conditions for maximum practical efficiency. Hence, in the following discussion we explore the factors that affect the efficiency of the bearing supported thin-film boiling engine above the Leidenfrost temperature only.

Assuming that the energy spent in pumping the liquid is negligible compared to the heat energy input, the efficiency ( $\eta$ ) of the thin-film boiling engine is calculated by  $\eta = P_o / \dot{Q}_{in}$ . For the hot plate used in our experiments,  $\dot{Q}_{in}$  varies between 400 and 500 W for temperatures between 250 and 400 °C. The maximum practical efficiency obtained in these experiments, which corresponds to the  $D = 500 \mu\text{m}$  design at  $H = 1.75 \text{ mm}$ , is approximately  $2 \times 10^{-6} \%$ . In the present proof-of-concept experiments, a significant amount of heat is lost to the surroundings. These energy losses can be mitigated by thermally insulating the working area and by using localized heating, for example, through selective substrate heating using microheaters [64,65]. By doing so, the energy input can be obtained close to the theoretical values ( $\dot{Q}_{in} = \rho_v L v_0 \pi R^2$ ), which are of the order of 10 W, thereby increasing the efficiency by an order of magnitude. Additional measures to increase the

practical efficiency of such engines can be evaluated from the analytical model. Keeping the basic substrate design features the same and using the expressions for torque (Eq. (7)), angular speed (Eq. (8)), vapor layer thickness (Eq. (9)) and heat input ( $\dot{Q}_{in} = \rho_v L v_0 \pi R^2$ , with  $v_0 = k \Delta T / \rho_v L h_v$ ), above the Leidenfrost temperature the efficiency will depend on the following key properties:

$$\eta \propto \left[ \frac{1}{\rho_l^{1/2} k^{3/8}} \left( \frac{\mu_v}{\rho_v L} \right)^{5/8} \right] \frac{P_v^{7/8}}{\Delta T^{3/8}} \frac{1}{\epsilon^{1/2} R^{5/4}} \quad (17)$$

From expression (17), the efficiency of the engine depends primarily on four factors: (1) heat source temperature or wall superheat  $\Delta T$ , (2) pressure in the vapor layer, or the pressure in the liquid  $P_v$ , (3) device scale and (4) thermophysical properties of the working liquid/vapor. The practical efficiencies obtained for varying temperature at each gap  $H$  did not show a significant variation and were within the experimental error. The analytical model also demonstrates a relatively weak dependence on temperature.

The effect of increased vapor pressure ( $P_v$ ) on the power output (and therefore, efficiency) has been demonstrated in this work. The vapor pressure increase was obtained using capillary pressure by reducing the gap between the rotor and the stator  $H$ . However, at the present device scale, the torque loss due to the vapor bubble formation limits a further decrease in  $H$  and, therefore, limits any further increase in the efficiency. With device sizes of the order of a few mm,  $H$  can be reduced to sub-mm scales without any bubble formation. Additionally, porous superhydrophilic rotors can ease liquid supply and ensure a continuously wetted thin-film of the liquid above the heated substrate. For example, with a continuously fed thin-liquid film of the order of 100  $\mu\text{m}$ , the efficiency can be increased almost by a factor of 10 (from expression (17)). Furthermore, reducing the liquid film thickness will also reduce viscous dissipation in the liquid, which will additionally enhance the power output; the energy loss due to viscous dissipation in the liquid has not been accounted for in the present analytical model.

A smaller device not only allows for practically increasing the vapor pressure, but also increases the efficiency directly from expression (17). Reducing the device scale by 2 increases the efficiency almost by the same factor. This dependency on  $R$  favors the development of mm and sub-mm scale engines. In conventional mechanical engines, at these scales, solid friction between the rotor and stator causes significant wear and loss. However, the vapor bearing in this thin-film boiling engine overcomes this challenge inherently in its operation. Additionally, a smaller device size will reduce the deformation of the liquid-vapor interface ( $\epsilon$ ), which will reduce the inertial resistance.

Based on the above examples, by thermally insulating the device and considering smaller device designs and higher liquid pressures, the practical efficiency can be increased by at least 3 orders of magnitude with water as a working substance. The working substance can also be changed considering the desired application. For example, ethanol, which has a Leidenfrost temperature of 180 °C, can be used as a working substance and provides an almost 2-fold increase in the efficiency over water (Table 1). Using working substances with a low Leidenfrost temperature (or in low ambient pressure environments [52]), such thin-film boiling engines can be developed for low grade thermal energy harvesting as an alternative to Organic Rankine Cycle engines for waste heat recovery [66,67]. For example, refrigerant R123 has a boiling point of 27.4 °C (Table 1). Therefore, its Leidenfrost temperature can be expected to be significantly lower than that of water and will allow thermal energy harvesting at much lower substrate temperatures. Similarly, as an example of application in space and planetary exploration, methane is abundantly present in liquid and vapor states on the surface of Saturn's moon, Titan. Using methane as a working liquid in those conditions can provide an almost 2-fold increase in the efficiency over water.

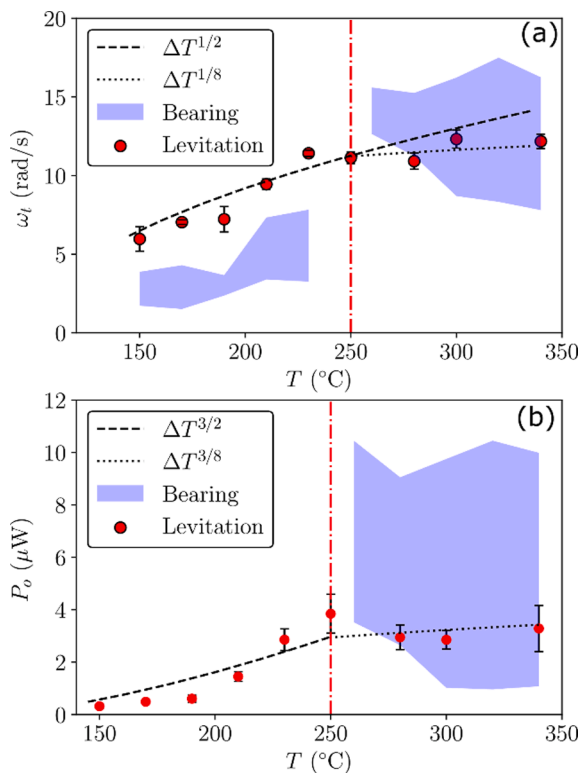


Fig. 11. Comparison of (a) terminal speed and (b) average power output obtained from the present fixed bearing system with the freely levitating rotor for the  $D = 500 \mu\text{m}$  substrate geometry. The dashed red line indicates the Leidenfrost temperature. The data for the freely levitating rotor is obtained from [50].

**Table 1**

General thermophysical properties of different potential working fluids for a thin-film boiling engine. The liquid properties are obtained just below the boiling point of the liquid. The properties for the vapor are obtained at the respective Leidenfrost temperatures, wherever available, or at the boiling point [68,69,70].

Fluid property	Water	Methanol	Ethanol	Methane on Titan	R123
Vapor dynamic viscosity $\mu_v$ ( $\mu\text{Pa s}$ )	14	15	17.5	9	15.5
Vapor thermal conductivity $k_v$ ( $\text{W m}^{-1} \text{K}^{-1}$ )	0.033	0.03	0.02	0.027	0.016
Liquid density $\rho_l$ ( $\text{kg m}^{-3}$ )	958	749	757	422.6	1457
Vapor density $\rho_v$ ( $\text{kg m}^{-3}$ )	0.6	0.9	1.11	1.3	4.1
Latent heat of vaporization $L$ ( $\text{kJ/kg}$ )	2264	1165	919	501	171
Boiling point $T_b$ ( $^{\circ}\text{C}$ )	100	64	78.2	-161.5	27.4
Leidenfrost point $T_L$ ( $^{\circ}\text{C}$ )	220	-	180	-	-
$\left[ \frac{1}{\rho_l^{1/2} k^{3/8} \rho_v} \left( \frac{\mu_v}{\rho_v L} \right)^{5/8} \right]$	1.58e-8	2.27e-8	2.94e-8	3.08e-8	2.70e-8

## 6. Conclusion

We presented a thin-film boiling engine with a mechanical power output control. The design comprises of a non-volatile solid rotor, coupled to a liquid volume via surface tension, suspended in a thin-film boiling state over a turbine-inspired substrate. The viscous drag from the vapor flow over the substrate produces torque on the rotors, which depends on the pressure in the vapor layer. By supporting the weight of the rotor using mechanical bearings, we manually alter the gap between the rotor and the substrate to alter the pressure in the liquid via the Laplace pressure. These changes in the liquid pressure alter the pressure in the vapor layer, which changes the rotation speed of the coupled solid rotor. We perform experiments above and below the Leidenfrost temperature and observe the variation in the power output for different gap between the rotor and the substrate across a temperature range of 150  $^{\circ}\text{C}$  to 350  $^{\circ}\text{C}$ . Despite the added solid friction from the bearings, we observe a significant enhancement in the rotation speed compared to levitation-based thin-film boiling engines for temperature above the Leidenfrost point. While the rotation speed increases with decreasing gap above the Leidenfrost temperature, the reverse trend is observed at temperatures below the Leidenfrost point. Random droplet ejection due to centrifugal forces hinder a direct measurement of torque. Therefore, using the analogy of a liquid bridge, we employ an analytical model to explain our experimental observations. We validate our analytical model with the experiments and obtain analytical estimates of the power output from the rotors. We overcome the challenge of a saturated power output in levitation-based engines and achieve an almost 4 times enhancement in the power output and practical efficiency. These design principles can be extrapolated to alternative liquid and solids to develop mm and sub-mm scale virtually frictionless engines. Potential applications of such engines can be in extreme environments with naturally occurring low pressures and high temperature differences, such as in space and planetary exploration or for terrestrial low-grade thermal energy harvesting as an alternative to Organic Rankine Cycles. Additionally, the inherent hydrodynamic lubrication provided by the thin-film boiling process can be used to overcome solid friction limitations at microscales for thermal energy harvesting.

## CRedit authorship contribution statement

**Prashant Agrawal:** Conceptualization, Methodology, Validation, Formal analysis, Investigation, Writing - original draft, Visualization. **Gary G. Wells:** Conceptualization, Visualization, Formal analysis, Data curation, Writing - review & editing, Funding acquisition. **Rodrigo Ledesma-Aguilar:** Conceptualization, Visualization, Formal analysis, Data curation, Writing - review & editing, Funding acquisition. **Glen McHale:** Supervision, Project administration, Funding acquisition, Writing - review & editing. **Khellil Sefiane:** Supervision, Project administration, Funding acquisition, Writing - review & editing.

## Declaration of Competing Interest

The authors declare that they have no known competing financial interests or personal relationships that could have appeared to influence the work reported in this paper.

## Acknowledgements

We would like to thank funding from Engineering and Physical Sciences Research Council (EPSRC), UK grants EP/P005896/1 and EP/P005705/1. We also thank Mr. Sam Hutchinson, Mr. Simon Neville and Mr. Phillip Donnelly for machining the substrates. The authors also acknowledge Prof. Anthony Walton, Dr. Adam Stokes, Dr. Jonathan Terry and Dr. Anthony Buchoux for useful discussions.

## Appendix A. Supplementary data

Supplementary data to this article can be found online at <https://doi.org/10.1016/j.apenergy.2021.116556>.

## References

- [1] Mueller RP, Sibille L, Mantovani J, Sanders GB, Jones CA. Opportunities and Strategies for Testing and Infusion of ISRU in the Evolvable Mars Campaign. American Institute of Aeronautics and Astronautics; 2015.
- [2] Hepp AF, Linne DL, Groth MF, Landis GA, Colvin JE. Production and use of metals and oxygen for lunar propulsion. AIAA/NASA/OAI Conf Adv SEI Technol 1991.
- [3] Montague M, McArthur GH, Cockell CS, Held J, Marshall W, Sherman LA, et al. The Role of Synthetic Biology for In Situ Resource Utilization (ISRU). *Astrobiology Nov. 2012*;12(12):1135–42.
- [4] Musk E. Making Humans a Multi-Planetary Species. *New Sp Jun. 2017*;5(2):46–61.
- [5] Graham JM. The Biological Terraforming of Mars: Planetary Ecosynthesis as Ecological Succession on a Global Scale. *Astrobiology 2004*;4(2):168–95.
- [6] Dreyer CB, Abbud-Madrid A, Atkinson J, Lampe A, Markley T, Williams H, et al. A new experimental capability for the study of regolith surface physical properties to support science, space exploration, and in situ resource utilization (ISRU). *Rev Sci Instrum 2018*;89(6).
- [7] Depcik C. Exploring the Potential of Combustion on Titan. *SAE Int J Aerosp 2018*; 11(1):27–45.
- [8] Bennett G. Space Nuclear Power: Opening the Final Frontier. 4th International Energy Conversion Engineering Conference and Exhibit (IECEC). American Institute of Aeronautics and Astronautics; 2006.
- [9] Wang Y, Zhou Z, Zhou J, Liu J, Wang Z, Cen K. Performance of a micro engine with heptane as working fluid. *Appl Energy 2011*;88(1):150–5.
- [10] Huesgen T, Ruhhammer J, Biancuzzi G, Woias P. Detailed study of a micro heat engine for thermal energy harvesting. *J Micromech Microeng 2010*;20(10): 104004.
- [11] Lee CH, Jiang KC, Jin P, Prewett PD. Design and fabrication of a micro Wankel engine using MEMS technology. *Microelectron Eng Jun. 2004*;73–74(1):529–34.
- [12] Sprague SB, Park SW, Walther DC, Pisano AP, Fernandez-Pello AC. Development and characterisation of small-scale rotary engines. *Int J Altern Propuls 2007*;1 (2–3):275–93.
- [13] Epstein AH. Millimeter-scale, micro-electro-mechanical systems gas turbine engines. *J Eng Gas Turbines Power 2004*;126(2):205.
- [14] Fu L, Feng Z, Li G. Investigation on design flow of a millimeter-scale radial turbine for micro gas turbine. *Microsyst Technol 2018*;24(5):2333–47.
- [15] Balanescu DT, Homutescu VM, Popescu A. Micro gas and steam turbines power generation system for hybrid electric vehicles. *IOP Conf Ser Mater Sci Eng. 2018*; 444(8).
- [16] Thapa S, Ogbonnaya E, Champagne C, Weiss L. MEMS-based boiler operation from low temperature heat transfer and thermal scavenging. *Micromachines 2012*;3(2): 331–44.

- [17] Lee C, Frechette LG. A silicon microturbopump for a rankine-cycle power generation microsystem part I: Component and system design. *J Microelectromech Syst* 2011;20(1):312–25.
- [18] Lee C, Liimini M, Frechette LG. A silicon microturbopump for a rankine-cycle power-generation microsystem part II: Fabrication and characterization. *J Microelectromech Syst* 2011;20(1):326–8.
- [19] Waits CM, McCarthy M, Ghodssi R. A microfabricated spiral-groove turbopump supported on microball bearings. *J Microelectromech Syst* 2010;19(1):99–109.
- [20] Peterson RB. Size limits for regenerative heat engines. *Microscale Thermophys Eng* 1998;2(2):121–31.
- [21] Ku ISY, Reddyhoff T, Holmes AS, Spikes HA. Wear of silicon surfaces in MEMS. *Wear* 2011;271(7–8):1050–8.
- [22] McCarthy M, Waits CM, Ghodssi R. Dynamic friction and wear in a planar-contact encapsulated microball bearing using an integrated microturbine. *J Microelectromech Syst* 2009;18(2):263–73.
- [23] Wang S, Han F, Sun B, Li H. Squeeze-film air damping of a five-axis electrostatic bearing for rotary micromotors. *Sensors (Switzerland)*. 2017;17(5).
- [24] Sun B, Han F, Li L, Wu Q. Rotation Control and Characterization of High-Speed Variable-Capacitance Micromotor Supported on Electrostatic Bearing. *IEEE Trans Ind Electron* 2016;63(7):4336–45.
- [25] Assadsangabi B, Tee MH, Takahata K. Electromagnetic Microactuator Realized by Ferrofluid-Assisted Levitation Mechanism. *J Microelectromech Syst* 2014;23(5):1112–20.
- [26] Yoxall BE, Chan ML, Harake RS, Pan T, Horsley DA. Rotary liquid droplet microbearing. *J Microelectromech Syst* 2012;21(3):721–9.
- [27] Chan ML, Yoxall B, Park H, Kang Z, Izyumin I, Chou J, et al. Design and characterization of MEMS micromotor supported on low friction liquid bearing. *Sens Actuat, A Phys* 2012;177:1–9.
- [28] Fréchet LG, Jacobson SA, Breuer KS, Ehrlich FF, Ghodssi R, Khanna R, et al. High-speed microfabricated silicon turbomachinery and fluid film bearings. *J Microelectromech Syst* 2005;14(1):141–52.
- [29] Leidenfrost JG. On the fixation of water in diverse fire. *Int J Heat Mass Transf* 1966;9(11):1153–66.
- [30] Biance AL, Clanet C, Quéré D. Leidenfrost drops. *Phys Fluids* 2003;15(6):1632–7.
- [31] Wildeman S, Sun C. Electric field makes Leidenfrost droplets take a leap. *Soft Matter* 2016;12(48):9622–32.
- [32] Piroird K, Clanet C, Quéré D. Magnetic control of Leidenfrost drops. *Phys Rev E - Stat Nonlinear, Soft Matter Phys* 2012;85(5):10–3.
- [33] Linke H, Alemán BJ, Melling LD, Taormina MJ, Francis MJ, Dow-Hygelund CC, et al. Self-propelled Leidenfrost droplets. *Phys Rev Lett*. 2006;96(154502).
- [34] Soto D, Lagubeau G, Clanet C, Quere D. Surfing on a herringbone. *Phys Rev Fluids*. 2016;1(013902).
- [35] Baier T, Dupeux G, Herbert S, Hardt S, Quéré D. Propulsion mechanisms for Leidenfrost solids on ratchets. *Phys Rev E - Stat Nonlinear, Soft Matter Phys* 2013;87(021001 (R)).
- [36] Bouillant A, Mouterde T, Bourrienne P, Lagarde A, Clanet C, Quéré D. Leidenfrost wheels. *Nat Phys* 2018;14:1188–92.
- [37] Dupeux G, Baier T, Bacot V, Hardt S, Clanet C, Quéré D. Self-propelling uneven Leidenfrost solids. *Phys Fluids*. 2013;25(051704).
- [38] Agapov RL, Boreyko JB, Briggs DP, Srijanto BR, Retterer ST, Collier CP, et al. Asymmetric wettability of nanostructures directs Leidenfrost droplets. *ACS Nano* 2014;8(1):860–7.
- [39] Lagubeau G, Le Merrer M, Clanet C, Quéré D. Leidenfrost on a ratchet. *Nat Phys* 2011;7(5):395–8.
- [40] Cousins TR, Goldstein RE, Jaworski JW, Pesci AI. A ratchet trap for Leidenfrost drops. *J Fluid Mech* 2012;696:215–27.
- [41] Agapov RL, Boreyko JB, Briggs DP, Srijanto BR, Retterer ST, Collier CP, et al. Length scale of Leidenfrost ratchet switches droplet directionality. *Nanoscale* 2014;6(15):9293–9.
- [42] Krumm C, Maduskar S, Paulsen AD, Anderson AD, Barberio NL, Damen JN, et al. Micro-ratcheted surfaces for a heat engine biomass conveyor. *Energy Environ Sci* 2016;9(5):1645–9.
- [43] Hai Jia Z, Yao Chen M, Tao Zhu H. Reversible self-propelled Leidenfrost droplets on ratchet surfaces. *Appl Phys Lett*. 2017;110(091603).
- [44] Dodd LE, Agrawal P, Parnell MT, Gerdali NR, Xu BB, Wells GG, et al. Low-Friction Self-Centering Droplet Propulsion and Transport Using a Leidenfrost Herringbone-Ratchet Structure. *Phys Rev Appl*. 2019;11(034063).
- [45] Arter JM, Cleaver DJ, Takashina K, Rhead AT. Self-propelling Leidenfrost droplets on a variable topography surface. *Appl Phys Lett*. 2018;113(243704).
- [46] Marín ÁG, Arnaldo del Cerro D, Römer GRBE, Pathiraj B, Huis in't Veld A, Lohse D. Capillary droplets on Leidenfrost micro-ratchets. *Phys Fluids*. 2012;24(12):122001.
- [47] Soto D, De Maleprade H, Clanet C, Quéré D. Air-levitated platelets: From take off to motion. *J Fluid Mech* 2017;814:535–46.
- [48] Xu H, Thissandier A, Zhao R, Tao P, Song C, Wu J, et al. Self-propelled rotation of paper-based Leidenfrost rotor. *Appl Phys Lett*. 2019;114(113703).
- [49] Wells GG, Ledesma-Aguilar R, McHale G, Sefiane K. A sublimation heat engine. *Nat Commun*. 2015;6(6390).
- [50] Agrawal P, Wells GG, Ledesma-Aguilar R, McHale G, Buchoux A, Stokes A, et al. Leidenfrost heat engine: Sustained rotation of levitating rotors on turbine-inspired substrates. *Appl Energy* 2019;240:399–408.
- [51] Orejon D, Sefiane K, Takata Y. Effect of ambient pressure on Leidenfrost temperature. *Phys Rev E - Stat Nonlinear, Soft Matter Phys* 2014;90(5):1–6.
- [52] Celestini F, Frisch T, Pomeau Y. Room temperature water Leidenfrost droplets. *Soft Matter* 2013;9(40):9535–8.
- [53] Sharon A, Bankoff SG. Destabilization of Leidenfrost boiling by a sudden rise of ambient pressure. *Chem Eng Sci* 1982;37(8):1173–9.
- [54] Gerdali NR, McHale G, Xu BB, Wells GG, Dodd LE, Wood D, et al. Leidenfrost transition temperature for stainless steel meshes. *Mater Lett* 2016;176:205–8.
- [55] Kwon HM, Bird JC, Varanasi KK. Increasing Leidenfrost point using micro-nano hierarchical surface structures. *Appl Phys Lett*. 2013;103(201601).
- [56] Del Cerro DA, Marín ÁG, Römer GRBE, Pathiraj B, Lohse D, Huis In'T Veld AJ. Leidenfrost point reduction on micropatterned metallic surfaces. *Langmuir*. 2012;28(42):15106–10.
- [57] Vakarelski IU, Marston JO, Chan DYC, Thoroddsen ST. Drag reduction by Leidenfrost vapor layers. *Phys Rev Lett*. 2011;106(214501).
- [58] Vakarelski IU, Patankar NA, Marston JO, Chan DYC, Thoroddsen ST. Stabilization of Leidenfrost vapour layer by textured superhydrophobic surfaces. *Nature* 2012;489(7415):274–7.
- [59] Dupeux G, Bourrienne P, Magdelaine Q, Clanet C, Quéré D. Propulsion on a superhydrophobic ratchet. *Sci Rep*. 2014;4(5280).
- [60] Perrard S, Couder Y, Fort E, Limat L. Leidenfrost levitated liquid tori. *EPL* 2012;100(5):54006.
- [61] Celestini F, Frisch T, Cohen A, Raufaste C, Duchemin L, Pomeau Y. Two dimensional Leidenfrost droplets in a Hele-Shaw cell. *Phys Fluids* 2014;26(3):032103.
- [62] Fortes MA. Axisymmetric liquid bridges between parallel plates. *J Colloid Interface Sci* 1982;88(2):338–52.
- [63] Bourrienne P, Lv C, Quéré D. The cold Leidenfrost regime. *Sci Adv*. 2019;5.
- [64] Dodd LE, Wood D, Gerdali NR, Wells GG, McHale G, Xu BB, et al. Low friction droplet transportation on a substrate with a selective Leidenfrost effect. *ACS Appl Mater Interfaces* 2016;8(34):22658–63.
- [65] Dodd LE, Agrawal P, Gerdali NR, Xu BB, Wells GG, Martin J, et al. Planar selective Leidenfrost propulsion without physically structured substrates or walls. *Appl Phys Lett*. 2020;117(081601).
- [66] Freeman J, Hellgardt K, Markides CN. An assessment of solar-powered organic Rankine cycle systems for combined heating and power in UK domestic applications. *Appl Energy* 2015;138:605–20.
- [67] Uusitalo A, Honkatukia J, Turunen-Saaresti T. Evaluation of a small-scale waste heat recovery organic Rankine cycle. *Appl Energy* 2017;192:146–58.
- [68] National Institute of Standards and Technology Chemistry WebBook. US Department of Commerce. <https://webbook.nist.gov/chemistry/fluid/>.
- [69] Vargaftik N. Handbook of Physical Properties of Liquids and Gases. Hemisphere, New York, NY., 1975.
- [70] Baumeister KJ, Henry RE, Simon FF. Role of the surface in the measurement of the Leidenfrost temperature. New York: Augment. Convect. Heat mass Transf. ASME Winter Annu. Meet; 1970.